Science Advances
AAAS

advances.sciencemag.org/cgi/content/full/6/14/eaaz0094/DC1

Supplementary Materials for

Massive generation of metastable bulk nanobubbles in water by external electric fields

Mohammad Reza Ghaani*, Peter G. Kusalik, Niall J. English*

*Corresponding author. Email: mohammad.ghaani@ucd.ie (M.R.G.); niall.english@ucd.ie (N.J.E.)

Published 1 April 2020, *Sci. Adv.* **6**, eaaz0094 (2020)
DOI: 10.1126/sciadv.aaz0094

This PDF file includes:

Section 1: Electric-Field Modeling and Energy Consumption

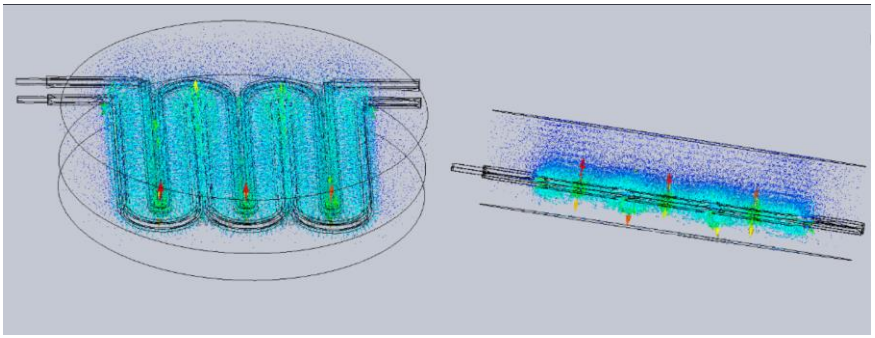

Figure S1: Finite-element simulation of extraneous electric-field distribution inside water (in which the plastic holder is immersed- cf. Fig. 1) from the applied 60 V DC field. The field intensity is reasonably uniform inside the liquid itself. The EMS package in SOLIDWORKS software was used.

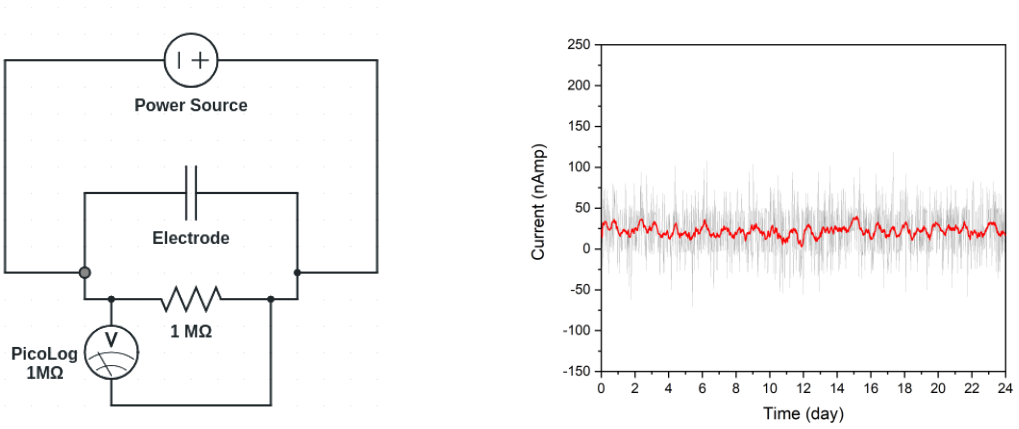

Figure S2: Equivalent circuit and *I-t* graph of the designed electrode during 60 V-induced nano-bubble generation. The calculated current based on the logged voltage is very low, but the average of this oscillation during 24 hours is 22 nAmp, which means it is required to add 1.9 mC to the capacitor to reach the equivalent energy. In any event, this is also the lower resolution limit of the current meter, so the energy is actually probably a good deal lower than this "upper limit". Thus, here, the total energy to form nano-bubbles over 24 hours will be:

$$U = \left(\frac{qV}{2}\right) = \left(\frac{1}{2} \times (1.9 \times 10^{-3}) \times 30\right) = 29mJ$$

Section 2: Lateral Dipolar Interactions in Spherical Nanobubbles

Our theoretical model will assume that nanobubbles are perfectly spherical and are characterized by a sharp, well-defined air-water interface. It has been well established by both experiments (*35*, *36*) and simulations (*36–44*) that the air-water interface is a structured environment in which the water molecules have preferred orientations (*i.e.*, hydrogen-bond arrangements). Simulations using both *ab-initio* and classical potential models have been performed for the air-water interface, and while there has been disagreement on the value of the surface potential that arises (*40–47*), studies are in agreement that there is a non-zero polarisation of the surface. Simulations using classical models have predicted that this structure gives rise a surface potential (a Galvanic potential difference) of about -0.6 V (*40*, *41*). Since in the present analysis, we are only interested in the long-range interactions of this surface structure (*i.e.*, where the size of the nanobubble is large relative to the width of the interface), it will be sufficient to describe the effects as arising from a set of surface dipole moments (*i.e.*, first moments of a surface charge distribution (*37*)). In this model, we need only to consider the component, μ, of the dipole moments perpendicular to the surface of the sphere, as we can assume that all other components will average to zero. The model then becomes a spherical shell of dipole moments at a radius R with a uniform (surface) density, ρ_s, where the dipoles all point away from the centre of the sphere, as shown in Fig. S3.

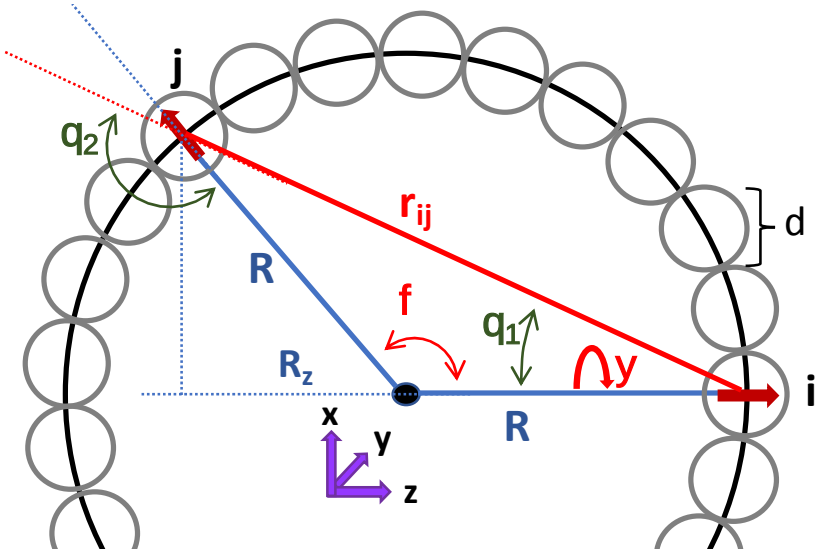

Figure S3. Schematic diagram showing the present model and its associated variables.

We now proceed to determine the lateral interactions between the dipoles within the spherical shell following a simplified version (achieved by setting r=R) of the development used by Kusalik and Patey (*48*) to determine local electric fields in electrolyte solutions (compare Fig. 2 of Ref. 14 with Fig. S3). It then follows that:

$$r_{ij}^{\ 2} = 2R^2(1 - cos\phi)\ , \qquad (1)$$

and eqn. (28) of Ref. 14 becomes

$$u_{ij}(R,\phi) = \frac{\mu^2}{2}\frac{(3 - cos\phi)}{(2R^2(1 - cos\phi))^{3/2}}\ . \qquad (2)$$

We define the lateral dipole interaction energy as

$$U^{lat}(R) = \sum_j u_{ij}(R,\phi) \ , \qquad (3)$$

where the sum is over all other dipoles in the spherical shell. For large R, we can take the neighbors j to be uniformly distributed in the shell and write (see eqn. (29) of Ref. 14):

$$\begin{aligned} U^{lat}(R) &= \rho_s \int_0^{2\pi} \int_{\phi_m}^{\pi} u_{ij}(R,\phi)(R^2 sin\phi \mathrm{d}\phi)\mathrm{d}\psi \\ &= 2\pi R^2 \rho_s \int_{\phi_m}^{\pi} u_{ij}(R,\phi) sin\phi \mathrm{d}\phi \\ &= 2\pi R^2 \rho_s \frac{\mu^2}{2} \int_{\phi_m}^{\pi} \frac{(3-cos\phi)sin\phi}{(2R^2(1-cos\phi))^{3/2}} \mathrm{d}\phi \quad . \end{aligned} \qquad (4)$$

Then integrating, and using that (cf. eqn (30) of Ref. 14)

$$\phi_m = cos^{-1}\left[\frac{2R^2 - d^2}{2R^2}\right] \ , \qquad (5)$$

where d is the diameter of the particles (or spacing of the dipoles), we can simplify to obtain

$$U^{lat}(R) = \frac{\pi \rho_s \mu^2}{2dR^2}(4R^2 - d^2) \ . \qquad (6)$$

In the limit of large R (i.e. R>>d), this simplifies to become

$$U^{lat}(R) = {2\pi\rho_s\mu^2}/{d} \ . \qquad (7)$$

Equation 7 is our first major result from the model showing that the lateral dipole interaction energy is independent of R, the size of the nanobubble.

To allow estimation of $U^{lat}(R)$, the total interaction of *i* with all *j* in the spherical shell, we will assume that the shell is composed of particles (dipoles) arrange on a square lattice with a diameter (spacing) of d. In this case $\rho_s = 1/d^2$, and

$$U^{lat}(R) = {2\pi\mu^2}/{d^3} \ . \qquad (8)$$

We remark that this form of the lateral interaction energy, in the presence of a nonzero dipole moment, will give rise to a nonlinear response to a uniform applied electric field. It also interesting to compare the value of $U^{lat}(R)$ with the (repulsive) arrangement where two dipoles are parallel and at a separation d; there $u_{ij} = \mu^2/d^3$. We can also compare eqn. (8) with the result of an infinite plane of particles with parallel dipole moments on a square lattice with density $\rho_s = 1/d^2$. We can proceed by summing over rings of dipoles at R, for which we have

$$U^{plane} = \sum_j u_{ij}(R) = \rho_s \int_d^{\infty} \frac{\mu^2}{R^3} 2\pi R \mathrm{d}R$$

$$= {2\pi\rho_s\mu^2}/{d} = {2\pi\mu^2}/{d^3}\,. \qquad (9)$$

Comparing eqns. (9) and (8), we see that the infinite plane and the spherical shell (for large R) yield the same result for the lateral dipole interaction energy. However, as we will see below, the spherical case results in a perpendicular force (that contributes to the pressure) that will not be present for the infinite plane.

In order to determine the pressure contribution, we first determine the force acting on particle (dipole) *i* due to the spherical shell of dipoles. We start with

$$\vec{f}_{ij}(R,\phi) = -\hat{r}_{ij}\frac{\mathrm{d}u_{ij}}{\mathrm{d}r_{ij}}\,, \qquad (10)$$

and proceed similarly to our approach above. Using eqn. (2), we immediately have

$$\vec{f}_{ij}(R,\phi) = \frac{\vec{r}_{ij}}{|r_{ij}|}\frac{3\mu^2}{2r_{ij}}(3-cos\phi)\,, \qquad (11)$$

where we note that this force is always repulsive. We are only interested in the *z* (i.e. perpendicular) component of this force, as the other components will sum to zero because of symmetry. Since r_z, the z-component of $\vec{r}_{ij}$, is given by (see Fig. S4):

$$r_z = R(1-cos\phi)\,, \qquad (12)$$

then

$$f_z(R,\phi) = \frac{3\mu^2}{2}\frac{r_z}{{r_{ij}}^5}(3-cos\phi)\,, \qquad (13)$$

and using eqns. (1) and (10) yields

$$f_z(R,\phi) = \frac{3\mu^2}{2}\frac{R(1-cos\phi)(3-cos\phi)}{(2R^2(1-cos\phi))^{5/2}}\,. \qquad (14)$$

We then obtain the total (perpendicular) force, $F^{lat}(R)$, acting on *i* due to the spherical shell by integrating (as in eqn. (4)):

$$F^{lat}(R) = 2\pi R^2\rho_s\int_{\phi_m}^{\pi} f_z(R,\phi)sin\phi\,\mathrm{d}\phi\,\,. \qquad (15)$$

Inserting eqn. (14) in eqn. (15) and simplifying, we obtain

$$F^{lat}(R) = \frac{3\pi\rho_s\mu^2}{4dR^3}(4R^2-d^2)\,\,, \qquad (16)$$

which in the limit of large R (*i.e.*, R>>d) and for a square lattice (i.e. $\rho_s = 1/d^2$) becomes

$$F^{lat}(R) = \frac{3\pi\mu^2}{d^3}\frac{1}{R}\,\,. \qquad (17)$$

We note that the force given by eqn. (17) is acting on particle *i* with area $A=d^2$, so we can immediately write the pressure contribution as

$$P^{lat}(R) = {}^{F}\!/_{A} = \frac{3\pi\mu^2}{d^5}\frac{1}{R} \ . \qquad (18)$$

Importantly, we see that this contribution to the effective pressure inside a nanobubble has the same dependence on size as the Laplace-pressure contribution (*49*, *50*). If we take *d*=2.8 Å, μ in D, and *R* is nm, then it is easily shown that

$$P^{lat}(R) = 5440\,{}^{\mu^2}\!/_{R} \text{ bar} \ . \qquad (19)$$

This can be compared to the Laplace-pressure contribution

$$P_{Laplace}(R) = {}^{1440}\!/_{R} \text{ bar} \ . \qquad (20)$$

Clearly, only modest values (*i.e.*, about 0.5 D) for the surface dipole moments are needed to the counter the effects of the Laplace pressure contribution.

It should also be noted that higher order terms, for example due to dipole-quadrupole interactions, can be similarly derived (cf. ref. 14). However, one finds that such terms have a stronger dependence on R, the bubble radius.

Section 3: NEMD Simulation of Nanobubbles

Molecular-dynamics simulations details

To study further size effects on nano-bubble behaviour, NEMD simulations was ran for two propane bubble diameters – 2.5 nm and 5 nm, with one (initially spherical) nano-bubble per simulation box. Methane bubbles were also simulated with 5 nm diameters. The simulation-box details are provided below in Table S1.

Table S1: Summary of the systems used in non-equilibrium molecular dynamics (NEMD) simulations

Gas	System	Bubble diameter (nm)	Box size (nm)	Total number of atoms	Total number of water molecules	Total number of propane molecules
Propane	Small	2.5	15.64×7.82×7.82	127,374	31,316	82
	Big	5.0	33.14×16.77×16.77	1,210,655	304,798	713
Methane	Big	5.0	33.14×16.77×16.77	1,148,326	285,364	1374

Orientation of surface-layer water molecules vis-à-vis the surface normal.

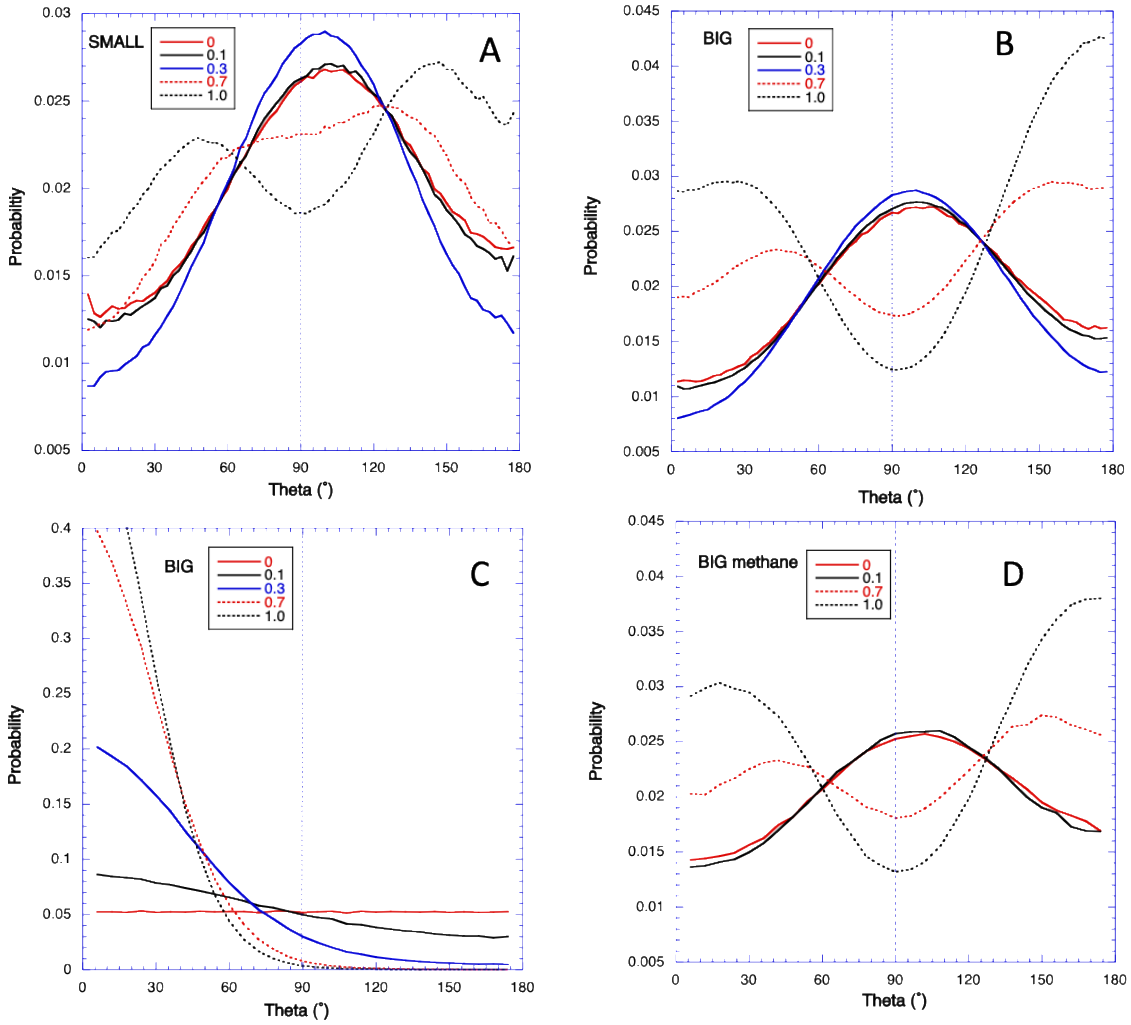

Figure S4: Probability distributions of the orientation of individual water molecule in the surface hydration layer relative to the surface normal, as a function of applied field strength, sampled from NEMD simulations. (A) For small system relative to surface normal, (B) for big system relative to surface normal, (C) for big system relative to field vector, and (D) for big methane system relative to surface normal. Here the surface normal is defined by the vector from the bubble centre of mass to the surface-bound water molecule. Here we note the asymmetric distribution (i.e. about 90˚) relative to the surface normal at zero field (indicating the polarization of the interface), and the non-linear response as manifested by the asymmetry of the distributions relative to the surface normal as well as the asymmetric shift notable particularly in the E=0.1 distribution in (C) relative to the field vector.

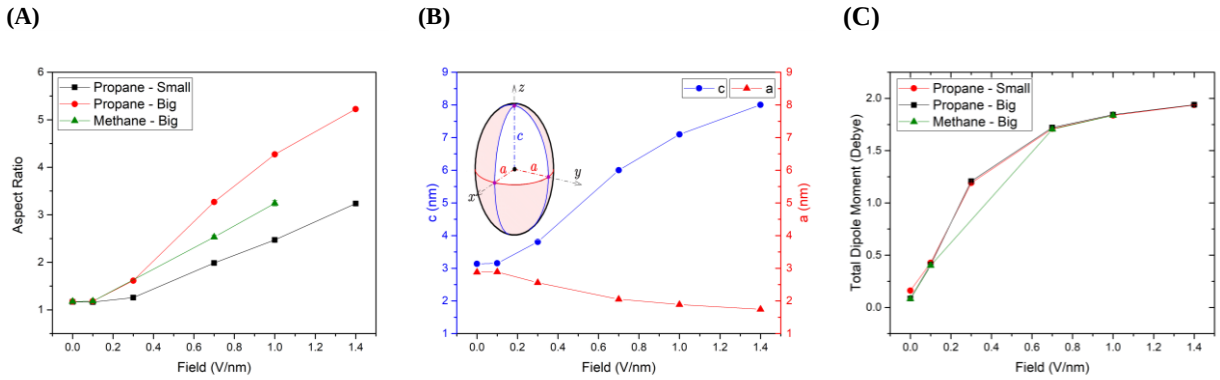

Figure S5. Bubble properties measured in NEMD simulations (A) The aspect ratio of bubbles during NEMD simulations as a function of applied field strength. (B) The propane bubble elongation presented in terms of *a* and *c* as a function of applied field strength. (C) The total dipole moment along the field direction of water molecules within the surface hydration layer, at different field strengths. All the results are presented for both small- and large-bubble systems in the case of propane, and for large methane bubbles, to see the effect of bubble size on behaviour.

Theoretical explanation of aspect ratios (elongation of bubbles along applied-field direction):

An expression for the electric-field square magnitude near an (initially) spherical void is (*26*, *27*):

$$E_{out}^2(r',\theta) = E_0^2\left(1 + (3\cos^2\theta + 1)\left(\frac{(\varepsilon-1)}{2\epsilon+1}\right)^2\frac{R^6}{r'^6} - (5\cos^2\theta - 1)\frac{R^3}{r'^3}\frac{(\varepsilon-1)}{2\epsilon+1}\right) \quad (21)$$

where θ is the angle between r and the applied electric field E_0. The volumetric force near the bubble is then (*27*):

$$F(r',\theta) \approx \frac{3}{2}\alpha\varepsilon\epsilon_0 E_0^2\frac{(\varepsilon-1)}{2\epsilon+1}\frac{R^3}{r'^4}\left(5\cos^2\theta - 1 - 2(3\cos^2\theta + 1)\frac{R^3}{r'^3}\frac{(\varepsilon-1)}{2\epsilon+1}\right) \quad (22)$$

When θ = 0, i.e., along the applied-field direction, the electric field is minimised, leading to a positive force, which points outwards, radially. As θ increases, the *de-facto* electric field E_{out} gets larger, with the force declining until it is negative (*27*). This results in stretching along the applied-field direction (*27*), as seen above from NEMD in Fig. S6.

Section 4: Drift-Velocities Analysis from NEMD Simulations

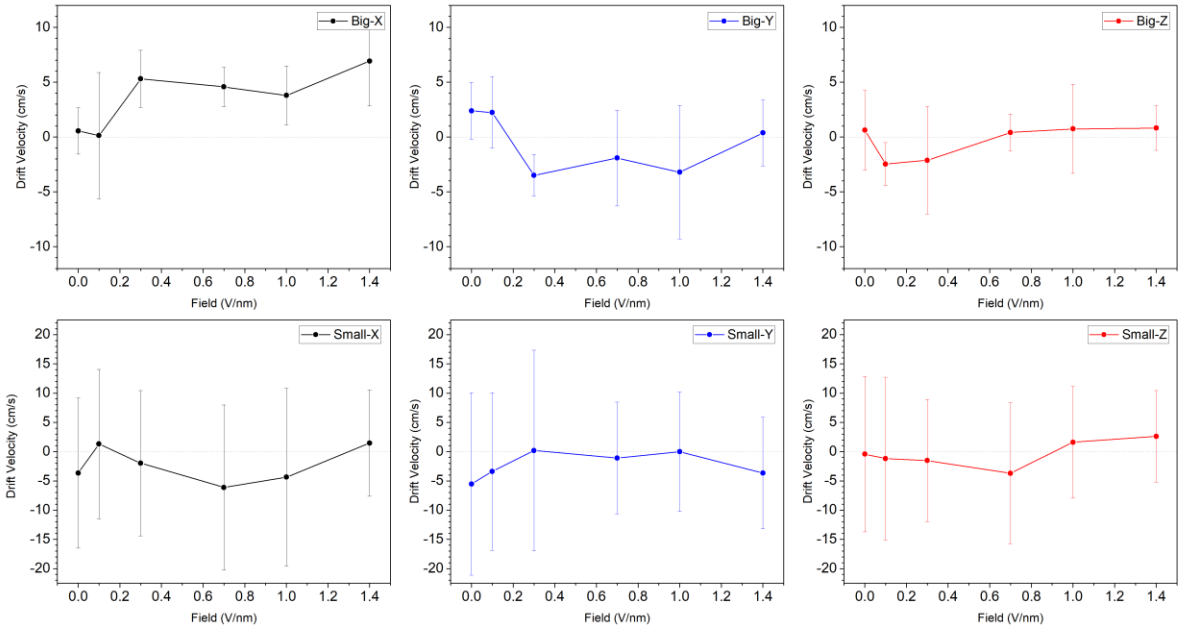

Figure S6. The calculated drift velocity as a function of the applied field (V/nm) for big- and small-propane-bubble systems. All of the observations were for 40-ns-long periods sampled hundreds of times with different time origins from four independent 50-ns trajectories. The depicted error bars are equal to one standard deviation. See Table S2 and S3 for further statistical analysis.

Table S2. The calculated drift velocities (cm/s) in all three directions as a function of applied field, where the field is applied in the X-direction

	Field (V/nm)	Number of replicae	X		Y		Z	
			Mean	St. Dev	Mean	St. Dev	Mean	St. Dev
Big	**0**	4	0.555	1.648	2.395	2.179	0.620	3.334
	0.1	4	0.139	5.504	2.234	2.971	-2.465	1.107
	0.3	4	5.307	1.819	-3.483	0.905	-2.125	4.570
	0.7	4	4.571	1.008	-1.916	4.243	0.416	1.340
	1.0	4	3.787	2.494	-3.204	5.946	0.745	3.850
	1.4	4	6.930	3.770	0.376	2.912	0.814	1.470
Small	**0**	4	-3.659	12.835	-5.524	15.609	-0.432	13.292
	0.1	4	1.298	12.775	-3.390	13.457	-1.187	13.925
	0.3	4	-1.964	12.424	0.190	17.156	-1.542	10.450
	0.7	4	-6.123	9.855	-1.091	6.060	-3.698	7.750
	1.0	4	-4.366	11.643	0.005	7.487	1.607	6.351
	1.4	4	1.460	5.161	-3.687	7.180	2.607	3.258

Table S3. Two-sample, two-tailed Student's t-test to evaluate the effect of field on drift velocity in the case of propane nano-bubbles in each field intensity, p-values less than 0.05 (95% confidence) are highlighted in red. It is clear that there are increasingly statistically-significant differences as a function of field intensity along the X-direction relative to the zero-field drift velocity, which agrees visually with the top left graph in Fig. S6 for the big-bubble system.

Field (V/nm)	0.0	0.1	0.3	0.7	1.0	1.4
0.0		0.89	0.01	0.01	0.07	0.02
0.1			0.12	0.16	0.27	0.09
0.3				0.51	0.36	0.47
0.7					0.58	0.27
1.0						0.21
1.4						

Field (V/nm)	0.0	0.1	0.3	0.7	1.0	1.4
0.0		0.60	0.86	0.77	0.94	0.49
0.1			0.73	0.39	0.54	0.98
0.3				0.62	0.79	0.63
0.7					0.83	0.22
1.0						0.40
1.4						

Drift velocity along X direction

Field (V/nm)	0.0	0.1	0.3	0.7	1.0	1.4
0.0		0.93	0.00	0.12	0.13	0.31
0.1			0.01	0.16	0.15	0.41
0.3				0.50	0.93	0.04
0.7					0.74	0.41
1.0						0.32
1.4						

Field (V/nm)	0.0	0.1	0.3	0.7	1.0	1.4
0.0		0.84	0.64	0.62	0.55	0.84
0.1			0.75	0.77	0.67	0.97
0.3				0.89	0.98	0.69
0.7					0.83	0.60
1.0						0.50
1.4						

Drift velocity along Y direction

Field (V/nm)	0.0	0.1	0.3	0.7	1.0	1.4
0.0		0.13	0.37	0.91	0.96	0.92
0.1			0.89	0.02	0.16	0.01
0.3				0.33	0.37	0.27
0.7					0.88	0.70
1.0						0.97
1.4						

Field (V/nm)	0.0	0.1	0.3	0.7	1.0	1.4
0.0		0.94	0.90	0.69	0.79	0.67
0.1			0.97	0.76	0.73	0.61
0.3				0.75	0.62	0.48
0.7					0.33	0.18
1.0						0.79
1.4						

Drift velocity along Z direction

Section 5: Electric-Field Intensities in NEMD

As mentioned in the main text, covalent bonds are prevented mechanically from rupture in the present simulations. Therefore, even for large fields approaching ~1.4 V/nm (where external forces are sometimes larger than 5% of the intrmolecular, regular intrinsic-system forces, and non-linear effects become apparent – as we have already seen for surface-molecular-dipole-distribution plots earlier). Although very interesting picosecond-scale non-equilibrium *ab-initio* MD on water break-up have been pioneered recently in such very large-magnitude fields, in various environments (*34*), these break-up events were not observed below ~3.5-4 V/nm, due to necessarily very short timescales (*34*). In any event, in the present study, water break-up, in terms of dissociation of chemical bonding, would not happen even for very large external fields, although we do not pursue NEMD with fields larger than 1.4 V/nm, so as to keep external-field forces at less than ~8-10% of intrinsic-system ones (*34*). The range up to 1.4 V/nm provides a compromise between being able to witness nanobubble-formation kinetics and structuring effects in the linear and non-linear régime over nanosecond-timescales.

In terms of computation of the intrinsic electric fields, this was performed by dividing the Coulombic-force vector at each charge site by its respective partial charge. This scalar intensity was then averaged to obtain for the intrinsic electric-field vector, and then coloured in a 'heat map' to show spatial variation in electric-field intensity. At no field application, typical intensities were found in the range of ~5-30 V/nm: in Fig. S7 a vs. b, it is seen that application of the external field leads to a substantial increase of field intensity (*i.e.*, field forces), with oval aspect – which is entirely consistent with electrostrictive-theory eqns. 21-22, and the aspect-ratio trends of Fig. S5.

(a)

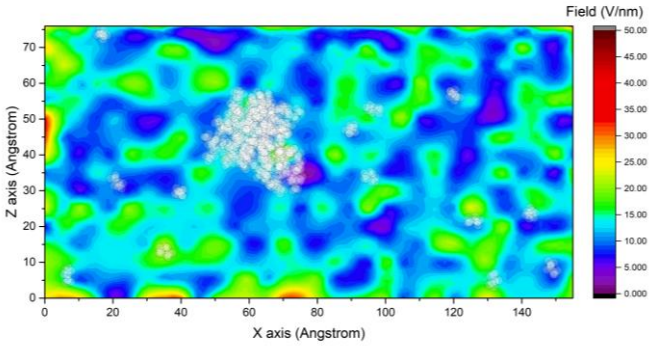

(b)

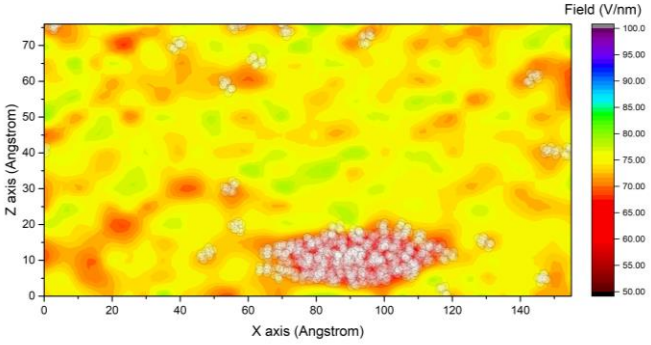

Fig. S7: Intrinsic electric-field intensities (reflective of Coulombic forces) for propane nano-bubbles in water under (a) zero-field conditions and (b) in 1.4 V/nm fields; white shows propane. white spheres represent propane molecules.

REFERENCES AND NOTES

1. J. R. T. Seddon, D. Lohse, W. A. Ducker, V. S. J. Craig, A deliberation on nanobubbles at surfaces and in bulk. *ChemPhysChem* **13**, 2179–2187 (2012).

2. D. Lohse, X. Zhang, Surface nanobubbles and nanodroplets. *Rev. Mod. Phys.* **87**, 981–1035 (2015).

3. M. Alheshibri, J. Qian, M. Jehannin, V. S. J. Craig, A history of nanobubbles. *Langmuir* **32**, 11086–11100 (2016).

4. J. Zhu, H. An, M. Alheshibri, L. Liu, P. M. J. Terpstra, G. Liu, V. S. J. Craig, Cleaning with bulk nanobubbles. *Langmuir* **32**, 11203–11211 (2016).

5. Y. Wang, B. Bhushan, Boundary slip and nanobubble study in micro/nanofluidics using atomic force microscopy. *Soft Matter* **6**, 29–66 (2010).

6. A. Agarwal, W. J. Ng, Y. Liu, Principle and applications of microbubble and nanobubble technology for water treatment. *Chemosphere* **84**, 1175–1180 (2011).

7. N. Mishchuk, J. Ralston, D. Fornasiero, Influence of very small bubbles on particle/bubble heterocoagulation. *J. Colloid Interface Sci.* **301**, 168–175 (2006).

8. K. K. Modi, A. Jana, S. Ghosh, R. Watson, K. Pahan, A physically-modified saline suppresses neuronal apoptosis, attenuates tau phosphorylation and protects memory in an animal model of Alzheimer's disease. *PLOS ONE* **9**, e103606 (2014).

9. A. K. A. Ahmed, C. Sun, L. Hua, Z. Zhang, Y. Zhang, T. Marhaba, W. Zhang, Colloidal properties of air, oxygen, and nitrogen nanobubbles in water: Effects of ionic strength, natural organic matters, and surfactants. *Environ. Eng. Sci.* **35**, 720–727 (2018).

10. E. Ruckenstein, Nanodispersions of bubbles and oil drops in water. *Colloids Surface A Physicochem. Eng. Asp.* **423**, 112–114 (2013).

11. M. Yarom, A. Marmur, Stabilization of boiling nuclei by insoluble gas: Can a nanobubble cloud exist? *Langmuir* **31**, 7792–7798 (2015).

12. J. Fraxedas, A. Verdaguer, F. Sanz, S. Baudron, P. Batail, Water nanodroplets confined in molecular nanobeakers. *Surf. Sci.* **588**, 41–48 (2005).

13. S. A. Peyman, J. R. McLaughlan, R. H. Abou-Saleh, G. Marston, B. R. G. Johnson, S. Freear, P. L. Coletta, A. F. Markham, S. D. Evans, On-chip preparation of nanoscale contrast agents towards high-resolution ultrasound imaging. *Lab Chip* **16**, 679–687 (2016).

14. S. Ljunggren, J. C. Eriksson, The lifetime of a colloid-sized gas bubble in water and the cause of the hydrophobic attraction. *Colloids Surfaces A Physicochem. Eng. Asp.* **129**–**130**, 151–155 (1997).

15. N. F. Bunkin, B. W. Ninham, P. S. Ignatiev, V. A. Kozlov, A. V. Shkirin, A. V. Starosvetskij, Long-living nanobubbles of dissolved gas in aqueous solutions of salts and erythrocyte suspensions. *J. Biophotonics* **4**, 150–164 (2011).

16. A. D. Usanov, S. S. Ulyanov, N. S. Ilyukhina, D. A. Usanov, Monitoring of changes in cluster structures in water under AC magnetic field. *Opt. Spectrosc.* **120**, 82–85 (2016).

17. R. Sander, in *NIST Chemistry WebBook, NIST Standard Reference Database Number 69* (National Institute of Standards and Technology, Gaithersburg MD, 2018), p. 20899; https://doi.org/10.18434/T4D303.

18. E. Wilhelm, R. Battino, R. J. Wilcock, Low-pressure solubility of gases in liquid water. *Chem. Rev.* **77**, 219–262 (1977).

19. M. R. Ghaani, N. J. English, A system, method and generator for generating nanobubbles or nanodroplets, UK IPO, 1816766.8 (2018).

20. Q. Wang, H. Zhao, N. Qi, Y. Qin, X. Zhang, Y. Li, Generation and stability of size-adjustable bulk nanobubbles based on periodic pressure change. *Sci. Rep.* **9**, 1118 (2019).

21. H.-F. Wang, L. Velarde, W. Gan, L. Fu, Quantitative sum-frequency generation vibrational spectroscopy of molecular surfaces and interfaces: Lineshape, polarization, and orientation. *Annu. Rev. Phys. Chem.* **66**, 189–216 (2015).

22. F. S. Cipcigan, V. P. Sokhan, A. P. Jones, J. Crain, G. J. Martyna, Hydrogen bonding and molecular orientation at the liquid–vapour interface of water. *Phys. Chem. Chem. Phys.* **17**, 8660–8669 (2015).

23. N. Nirmalkar, A. W. Pacek, M. Barigou, Interpreting the interfacial and colloidal stability of bulk nanobubbles. *Soft Matter* **14**, 9643–9656 (2018).

24. R. Vácha, O. Marsalek, A. P. Willard, D. Jan Bonthuis, R. R. Netz, P. Jungwirth, Charge transfer between water molecules as the possible origin of the observed charging at the surface of pure water. *J. Phys. Chem. Lett.* **3**, 107–111 (2011).

25. E. Amah, M. Janjua, P. Singh, Direct numerical simulation of particles in spatially varying electric fields. *Fluids* **3**, 52 (2018).

26. M. N. Shneider, M. Pekker, Cavitation in dielectric fluid in inhomogeneous pulsed electric field. *J. Appl. Phys.* **114**, 214906 (2013).

27. M. N. Shneider, M. Pekker, Pre-breakdown processes in a dielectric fluid in inhomogeneous pulsed electric fields. *J. Appl. Phys.* **117**, 224902 (2015).

28. N. Giri, M. G. Del Pópolo, G. Melaugh, R. L. Greenaway, K. Rätzke, T. Koschine, L. Pison, M. F. C. Gomes, A. I. Cooper, S. L. James, Liquids with permanent porosity. *Nature* **527**, 216–220 (2015).

29. J. L. F. Abascal, C. Vega, A general purpose model for the condensed phases of water: TIP4P/2005. *J. Chem. Phys.* **123**, 234505 (2005).

30. J. Wang, R. M. Wolf, J. W. Caldwell, P. A. Kollman, D. A. Case, Development and testing of a general amber force field. *J. Comput. Chem.* **25**, 1157–1174 (2004).

31. A. D. MacKerell Jr., D. Bashford, M. Bellott, R. L. Dunbrack, J. D. Evanseck, M. J. Field, S. Fischer, J. Gao, H. Guo, S. Ha, D. Joseph-McCarthy, L. Kuchnir, K. Kuczera, F. T. K. Lau, C. Mattos, S. Michnick, T. Ngo, D. T. Nguyen, B. Prodhom, W. E. Reiher, B. Roux, M. Schlenkrich, J. C. Smith, R. Stote, J. Straub, M. Watanabe, J. Wiórkiewicz-Kuczera, D. Yin, M. Karplus, All-atom empirical potential for molecular modeling and dynamics studies of proteins. *J. Phys. Chem. B* **102**, 3586–3616 (1998).

32. M. P. Allen, D. J. Tildesley, *Computer Simulation of Liquids* (Oxford Univ. Press, 2017).

33. M. R. Ghaani, N. J. English, Molecular dynamics study of propane hydrate dissociation: Nonequilibrium analysis in externally applied electric fields. *J. Phys. Chem. C* **122**, 7504–7515.

34. N. J. English, C. J. Waldron, Perspectives on external electric fields in molecular simulation: Progress, prospects and challenges. *Phys. Chem. Chem. Phys.* **17**, 12407–12440 (2015).

35. R. Vácha, S. W. Rick, P. Jungwirth, A. G. F. de Beer, H. B. de Aguiar, J.-S. Samson, S. Roke, The orientation and charge of water at the hydrophobic oil droplet–water interface. *J. Am. Chem. Soc.* **133**, 10204–10210 (2011).

36. R. Vácha, O. Marsalek, A. P. Willard, D. J. Bonthuis, R. R. Netz, P. Jungwirth, Charge transfer between water molecules as the possible origin of the observed charging at the surface of pure water. *J. Phys. Chem. Lett.* **3**, 107–111 (2012).

37. F. Tang, T. Ohto, T. Hasegawa, W. J. Xie, L. Xu, M. Bonn, Y. Nagata, Definition of free O–H groups of water at the air–water interface. *J. Chem. Theory Comput.* **14**, 357–364 (2018).

38. M. A. Wilson, A. Pohorille, L. R. Pratt, Surface potential of the water liquid–vapor interface. *J. Chem. Phys.* **88**, 3281–3285 (1988).

39. V. P. Sokhan, D. J. Tildesley, The free surface of water: Molecular orientation, surface potential and nonlinear susceptibility. *Mol. Phys.* **92**, 625–640 (1997).

40. J. R. Cendagorta, T. Ichiye, The surface potential of the water–vapor interface from classical simulations. *J. Phys. Chem. B* **119**, 9114–9122 (2015).

41. S. M. Kathmann, I.-F. W. Kuo, C. J. Mundy, G. K. Schenter, Understanding the surface potential of water. *J. Phys. Chem. B* **115**, 4369–4377 (2011).

42. K. Leung, Surface potential at the air−water interface computed using density functional theory. *J. Phys. Chem. Lett.* **1**, 496–499 (2010).

43. M. D. Baer, A. C. Stern, Y. Levin, D. J. Tobias, C. J. Mundy, Electrochemical surface potential due to classical point charge models drives anion adsorption to the air–water interface. *J. Phys. Chem. Lett.* **3**, 1565–1570 (2012).

44. R. C. Remsing, M. D. Baer, G. K. Schenter, C. J. Mundy, J. D. Weeks, The role of broken symmetry in solvation of a spherical cavity in classical and quantum water models. *J. Phys. Chem. Lett.* **5**, 2767–2774 (2014).

45. B. Sellner, M. Valiev, S. M. Kathmann, Charge and electric field fluctuations in aqueous NaCl electrolytes. *J. Phys. Chem. B* **117**, 10869–10882 (2013).

46. P. G. Kusalik, G. N. Patey, On the molecular theory of aqueous electrolyte solutions. IV. Effects of solvent polarizability. *J. Chem. Phys.* **92**, 1345–1358 (1990).

47. K. Yasui, T. Tuziuti, W. Kanematsu, Mysteries of bulk nanobubbles (ultrafine bubbles); stability and radical formation. *Ultrason. Sonochem.* **48**, 259–266 (2018).